IEEE Access
Multidisciplinary ⋮ Rapid Review ⋮ Open Access Journal

Received January 6, 2022, accepted February 11, 2022, date of publication February 15, 2022, date of current version March 7, 2022.

Digital Object Identifier 10.1109/ACCESS.2022.3151649

Celestial Spectrum Velocimetry With Non-Linear Fourier Phase Shift and Its CRLB

ZIJUN ZHANG[1], JIN LIU[1], AND XIAOLIN NING[2]
[1]College of Information Science and Engineering, Wuhan University of Science and Technology, Wuhan 430081, China
[2]School of Instrument Science and Optoelectronics Engineering, Beihang University, Beijing 100191, China

Corresponding author: Jin Liu (liujin@wust.edu.cn)

This work was supported by the National Natural Science Foundation of China under Grant 61873196 and Grant 61772187.

ABSTRACT To solve the problem of the non-linear Fourier phase shift caused by the wavelength shift in the celestial spectrum velocimetry, a celestial spectrum velocimetry method based on non-uniform discrete Fourier transform and compressed sensing is proposed. First, according to the properties of the non-uniform discrete Fourier transform with non-periodic celestial spectra, the non-linear relationship between the spectral wavelength shift and the Fourier phase shift is deduced theoretically. And then, the discrete cosine transform is used to decompose and reconstruct the spectrum to construct the phase dictionary of the non-periodic spectrum. In this dictionary, the spectral wavelength shift has a non-linear relationship with the Fourier phase shift. Finally, the non-uniform Fourier transform matrix is used as the measurement matrix. And the Doppler wavelength shift is estimated by using a non-linear and super-resolution matching algorithm to estimate the velocimetry. Experimental results show that when the spacecraft's velocity is high, the celestial spectrum velocimetry method with non-linear Fourier phase shift (CSV-NFPS) can effectively measure the velocity from the spectrum, and its accuracy approaches the theoretical Cramer-Rao lower bounds (CRLB). Compared with the traditional Taylor method, the CSV-NFPS has an average accuracy improvement of 16.18% and a computational complexity reduction of 25.07%. In short, our method eliminate the non-linear bias in the celestial spectrum velocimetry and reduce a certain computational complexity.

INDEX TERMS Celestial navigation, compressed sensing, CRLB, Fourier transform, phase shift.

I. INTRODUCTION

Deep space exploration refers to the exploration and observation of the moon and beyond. Compared with the near-Earth space exploration missions, there are still many difficulties in the deep space exploration missions that need to be broken through, such as the long-distance and the large time delay. Autonomous celestial navigation can solve these problems, as it relies on real-time celestial information measurement instead of the velocity and the position information given by the ground stations. It has the advantages of low time delay, high accuracy, strong anti-interference ability, and navigation errors that do not accumulate with time [1], [2]. Autonomous navigation improves the success rate of spacecraft in completing unique and complex tasks [3].

Celestial navigation measurements include three types: angle measurement [4], distance measurement [5] and velocimetry [6]. The traditional celestial navigation obtains the velocity information indirectly by solving the angle information and the distance information. [7], [8]. The accurate velocity information is difficult to obtain directly.

The wavelength shift information can be obtained from the celestial optical information. By analyzing the information, the real-time velocity of the spacecraft can be obtained [9]. Stars in space can be used as the navigation light source [10]. By observing three or more navigational celestial bodies simultaneously, the three-dimensional velocity vector of the spacecraft can be obtained. After the real-time and high-accuracy velocity estimation is achieved in autonomous navigation [11], [12], it can be combined with the angle and range navigation methods to further improve the performance of autonomous navigation [13]–[16]. The idea of using the spectral variation of the Doppler effect for navigation has long been proposed [17], and a lot of research has been done on the measurement of radial velocity (RV) of celestial bodies [18]. The velocimetry navigation mainly focuses on the measurement of RV using spectrum. The common method is to synthesize a high signal-to-noise ratio standard spectrum

The associate editor coordinating the review of this manuscript and approving it for publication was Lorenzo Mucchi.

template, and then match the measured spectrum with the template spectrum to derive the RV [19], [20]. In terms of measurement principle, these algorithms can be divided into the non-transform domain and transform domain. The non-transform domain methods include the cross-correlation function (CCF), the least square fitting [20], the differential estimation method [20], and the Gaussian processes [21]. The Taylor method (Taylor FFT) and the Bispectrum method are typical transform domain methods. The non-transform domain method is affected by the wavelength resolution and the frequency resolution. Generally, high wavelength resolution is benefit to the velocimetry accuracy. However, the wavelength resolution of the spectrometer at spacecraft is low due to the limitation of technology [22]. The Fourier transform domain method is robust to wavelength resolution. It is worth mentioning that the amount of computation of the Taylor method is far fewer than that of the bispectrum method. Thus, the bispectrum method is not suitable for spacecraft.

Zhang used compressed sensing to optimize the Taylor method, and proposed the mirror NDFT-CS method [23]. However, in the simulation of the mirror NDFT-CS method, it is unpractical to directly move the wavelength of the spectrum instead of the change of flux. In the above methods, the Fourier phase shift is assumed as linear [24]. However, the Fourier phase shift of the non-periodic celestial spectrum is non-linear. In addition, the non-linear velocimetry bias increases with the shortening of the celestial spectrum band [19]. The wavelength band of the spectrometer in spacecraft is short, which causes a large velocimetry bias. Several existing algorithms [19], [20] do not consider the influence of this bias, whichl affect the high-precision Doppler RV estimation to a certain degree. To improve the stability and accuracy of velocimetry, it is requirable to eliminate this non-linear bias.

In recent years, compressed sensing (CS) has become a research hotspot in the field of signal processing due to its strong non-linear signal processing capabilities [25], [26]. To solve the problem of the non-linear Fourier phase shift, we introduce CS into the celestial spectrum velocimetry, and propose the celestial spectrum velocimetry method with non-linear Fourier phase shift (CSV-NFPS). The core of this ideal is that the non-linear Fourier phase shift is approximated by the phase dictionary of the non-periodic spectrum. First, we use discrete cosine transform (DCT) and non-uniform discrete Fourier transform (NDFT) to generate a series of Doppler spectra that construct a phase dictionary of the non-periodic celestial spectrum. And then we design the low-frequency measurement matrix with NDFT to generate the observation vector. Finally, the non-linear and super-resolution matching algorithm is used to derive velocity. Besides, we deduce the Cramer-Rao lower bound (CRLB) of the celestial spectrum velocity.

The structure of the remainder of this paper is as follows. Section 2 introduces the principles of celestial spectrum velocimetry. The property of non-linear Fourier phase shift of non-periodic spectrum is given in Section 3. The celestial spectrum velocimetry method with non-linear Fourier phase shift is proposed in Section 4. The CRLB for the celestial spectrum velocimetry is deduced in Section 5. The simulation results in Section 6 demonstrate the accuracy, real-time and low requirements for spectrometer of the CSV-NFPS. Finally, conclusions are summarized in Section 7.

II. PRINCIPLE OF CELESTIAL SPECTRUM VELOCIMETRY

In this section, we review the basic principle of celestial spectrum velocimetry. When the spacecraft moves away from the light source, the spectrum moves to red; when the spacecraft approaches the light source, the spectrum moves to blue. This phenomenon is the Doppler effect of light. This article aims to analyze the RV between spacecraft and light source. The relationship between the RV and the Doppler wavelength shift is as follows (without considering the influence of relativity):

$$\frac{1}{\lambda_s} = \frac{1}{\lambda_0}(1 + \frac{v}{c}) \tag{1}$$

where λ_0 is the original spectral wavelength, λs is the Doppler spectral wavelength, v is the RV between the light source and the spacecraft, and c is the speed of light.

Taking the logarithm of both sides of (1), we get (2) as follows:

$$\ln\lambda_s = \ln\lambda_0 - \ln(1 + \frac{v}{c}) \tag{2}$$

The relationship between the original spectrum and the Doppler spectrum can be expressed as follows:

$$\boldsymbol{s}(\ln\lambda_s) = \boldsymbol{s}[\ln\lambda_0 - \ln(1 + \frac{v}{c})] \tag{3}$$

where $\boldsymbol{s}(\ln\lambda_0)$ and $\boldsymbol{s}(\ln\lambda_s)$ are the original and the Doppler spectra, respectively.

III. NONLINEAR FOURIER PHASE SHIFT OF THE NON-PERIODIC SPECTRUM

The Fourier phase shift between the shifted periodic spectrum and the original spectrum is linear. However, the celestial spectrum is finite and non-periodic, which results in non-linear Fourier phase shift. In this section, we prove the property of the non-linear Fourier phase shift of the non-periodic spectrum.

Property 1: The Fourier phase shift between the Doppler spectrum and the original spectrum is non-linear.

Proof: The original celestial spectrum, $\boldsymbol{s}(\ln\lambda_0)$, $\lambda_0 \in [\Lambda_a, \Lambda_b]$, is non-periodic and finite. Assume that Λ_a and Λ_b are the starting wavelength and the cut-off wavelength of the spectrum, respectively. $s(\ln\lambda s)$, $\lambda_s \in [\frac{c\Lambda_\alpha}{c+v}, \frac{c\Lambda_b}{c+v}]$, denotes for the Doppler spectrum.

For periodic spectrum, that is, $\boldsymbol{s}(\ln\lambda_0) = \boldsymbol{s}(\ln\lambda_0 + \ln\Lambda_b - \ln\Lambda_a)$, the Fourier phase shift between the Doppler spectrum and the original spectrum is linear (4) holds

$$\mathscr{F}\{\boldsymbol{s}(\ln\lambda_s)\} e^{j\omega\tau} = \mathscr{F}\{\boldsymbol{s}(\ln\lambda_0 - \tau)\} e^{j\omega\tau}$$

$$
\begin{aligned}
&= \int_{\ln \Lambda_a}^{\ln \Lambda_b} \boldsymbol{s}(\ln \lambda - \tau) e^{-j\omega(\ln \lambda - \tau)} d(\ln \lambda) \\
&= \int_{\ln \Lambda_a - \tau}^{\ln \Lambda_b} \boldsymbol{s}(\ln \lambda) e^{-j\omega \ln \lambda} d(\ln \lambda) \\
&\quad - \int_{\ln \Lambda_b - \tau}^{\ln \Lambda_b} \boldsymbol{s}(\ln \lambda) e^{-j\omega \ln \lambda} d(\ln \lambda) \\
&= \int_{\ln \Lambda_a - \tau}^{\ln \Lambda_b} \boldsymbol{s}(\ln \lambda) e^{-j\omega \ln \lambda} d(\ln \lambda) \\
&\quad - \int_{\ln \Lambda_b - (\ln \Lambda_b - \ln \Lambda_a) - \tau}^{\ln \Lambda_b - (\ln \Lambda_b - \ln \Lambda_a)} \boldsymbol{s}(\ln \lambda) e^{-j\omega \ln \lambda} d(\ln \lambda) \\
&= \int_{\ln \Lambda_a - \tau}^{\ln \Lambda_b} \boldsymbol{s}(\ln \lambda) e^{-j\omega \ln \lambda} d(\ln \lambda) \\
&\quad - \int_{\ln \Lambda_a - \tau}^{\ln \Lambda_a} \boldsymbol{s}(\ln \lambda) e^{-j\omega \ln \lambda} d(\ln \lambda) \\
&= \int_{\ln \Lambda_a}^{\ln \Lambda_b} \boldsymbol{s}(\ln \lambda) e^{-j\omega \ln \lambda} d(\ln \lambda) \\
&= \mathscr{F}\{\boldsymbol{s}(\ln \lambda_0)\}
\end{aligned} \tag{4}
$$

where τ is the logarithmic wavelength shift, whose expression is given as follows:

$$\tau = \ln(1 + \frac{v}{c}) \tag{5}$$

For the non-periodic spectrum, the above equation does not hold. The reason is that $\boldsymbol{s}(\ln\lambda_0) \neq \boldsymbol{s}(\ln\lambda_0 + \ln\Lambda_b - \ln\Lambda_a)$. The phase shift between $\boldsymbol{s}(\ln\lambda_0)$ and $\boldsymbol{s}(\ln\lambda_s)$ is non-linear:

$$
\begin{aligned}
\mathscr{F}\{\boldsymbol{s}(\ln \lambda_s)\} e^{j\omega\tau} &= \int_{\ln \Lambda_a - \tau}^{\ln \Lambda_b} \boldsymbol{s}(\ln \lambda) e^{-j\omega \ln \lambda} d(\ln \lambda) \\
&\quad - \int_{\ln \Lambda_b - \tau}^{\ln \Lambda_b} \boldsymbol{s}(\ln \lambda) e^{-j\omega \ln \lambda} d(\ln \lambda) \\
&\neq \int_{\ln \Lambda_a - \tau}^{\ln \Lambda_b} \boldsymbol{s}(\ln \lambda) e^{-j\omega \ln \lambda} d(\ln \lambda) \\
&\quad - \int_{\ln \Lambda_a - \tau}^{\ln \Lambda_a} \boldsymbol{s}(\ln \lambda) e^{-j\omega \ln \lambda} d(\ln \lambda) \\
&= \mathscr{F}\{\boldsymbol{s}(\ln \lambda_0)\}
\end{aligned} \tag{6}
$$

Therefore, the phase shift between the original spectrum and the Doppler spectrum is non-linear.

IV. CELESTIAL SPECTRUM VELOCIMETRY WITH NON-LINEAR FOURIER PHASE SHIFT

The CS-based celestial spectrum velocimetry for non-periodic spectrum is proposed in this section. In the previous section, we have proved the property of non-linear phase shift caused by non-periodic spectral wavelength shift. The traditional Taylor method explores linear time shift property to derive the RV. However, the non-linear phase shift has a certain impact on the accuracy of the traditional Taylor method. To eliminate the influence of non-linear phase shift between the Doppler spectrum and the original spectrum, we introduce compressed sensing. The non-linear phase shift is segmented by the phase dictionary of the non-periodic spectrum. The non-linear and super-resolution matching algorithm is used to obtain accurate estimation. In this method, the bias of non-linear phase shift caused by non-periodic spectral wavelength shift is avoided. Firstly, the basic principles of NDFT and non-linear phase shift in the Taylor method are introduced. Then the low-frequency matrix, the zero phase shift atom, the observation vector and the phase dictionary are given in compressed sensing. Finally, the algorithm is summarized.

The diagram of the CSV-NFPS is shown as Figure 1, where $\otimes$ denotes for the matrix multiplication. The algorithm consists of four modules: (1) the design of the low-frequency Fourier measurement matrix (yellow underpainting), (2) the construction of the phase dictionary (green underpainting), (3) the obtainment of the observation vector (purple underpainting), and (4) the acquisition of Doppler velocity using the non-linear and super-resolution matching algorithm (red underpainting). And Figure 1(a) is a module of construction of phase dictionary of Figure 1(b) (white underpainting).

The construction of measurement matrix and dictionary is completed on grand in advance; the acquisition of the measured spectrum and the solution of velocity using the non-linear and super-resolution matching algorithm operate at the spacecraft. Our goal is to fast derive the Doppler velocity after the spectrum collection. Hence, our optimization objective is to decrease the computational load of the fourth module.

The details of four modules of the CSV-NFPS are given as follows.

A. ANALYSIS OF THE NON-LINEAR PHASE IN THE NDFT TAYLOR METHOD

In this section, we analyse the non-linear phase shift in the NDFT Taylor method. Assume that the original spectrum is $\boldsymbol{s}(\ln\lambda_n)$, where λ_n is the wavelength of the spectrum, $n = 0, 1, 2, 3 \ldots N-1$. N *is* the number of sampling points of the spectrum. $\boldsymbol{S}(k)$ and $\boldsymbol{\phi}(k)$ are the amplitude and phase of the NDFT of $\boldsymbol{s}(\ln\lambda_n)$, respectively, where k is the discrete frequency.

The expression of the NDFT of $\boldsymbol{s}(\ln\lambda_n)$ is shown as follows:

$$\boldsymbol{S}(k)e^{j\boldsymbol{\varphi}(k)} = \sum_{n=1}^{N-2} (\ln \lambda_{n+1} - \ln \lambda_{n-1})\, \boldsymbol{s}(\ln \lambda_n) e^{-\frac{j2\pi k \ln \lambda_n}{\ln \Lambda_b - \ln \Lambda_a}} \tag{7}$$

The Doppler spectrum received by the spacecraft is $\boldsymbol{p}(\ln\lambda_n)$. $\boldsymbol{P}(k)$ and $\boldsymbol{\theta}(k)$ are the amplitude and phase of the NDFT of $\boldsymbol{p}(\ln\lambda_n)$, respectively. The expression of the NDFT of $\boldsymbol{p}(\ln\lambda_n)$ is shown as follows:

$$\boldsymbol{P}(k)e^{j\boldsymbol{\theta}(k)} = \sum_{n=1}^{N-1} (\ln \lambda_{n+1} - \ln \lambda_{n-1})\, \boldsymbol{p}(\ln \lambda_n) e^{-\frac{j2\pi k \ln \lambda_n}{\ln \Lambda_b - \ln \Lambda_a}} \tag{8}$$

We assume that the relationship between $\boldsymbol{s}(\ln\lambda_n)$ and $\boldsymbol{p}(\ln\lambda_n)$ is as follows:

$$\boldsymbol{p}(\ln \lambda_n) = \kappa[\boldsymbol{s}(\ln \lambda_n - \tau)] + \boldsymbol{\omega}(n) \tag{9}$$

where κ is the amplitude factor, $\omega(n)$ is the noise.

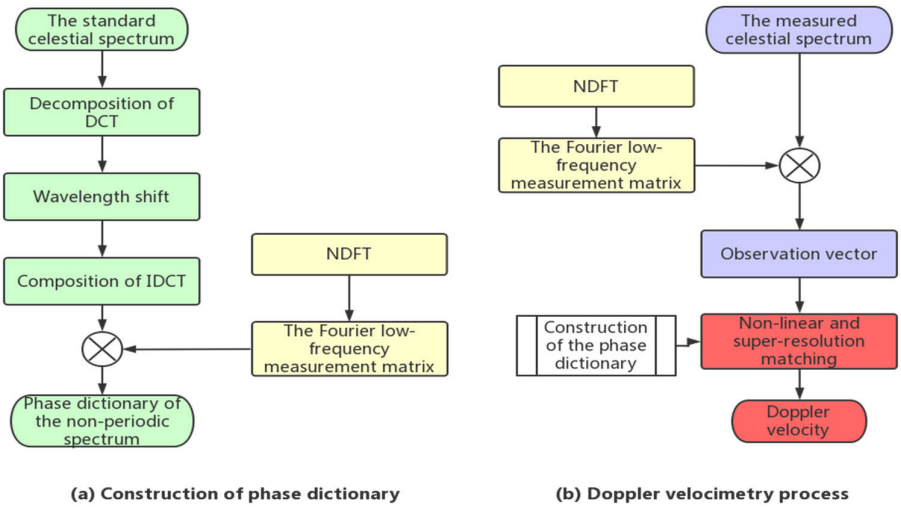

FIGURE 1. Diagram of the CSV-NFPS. (a) is the process of construction a dictionary, just on the ground. (b) is the velocimetry process on spacecraft.

The displacement τ and the gain κ can be derived by (10) [24]

$$E^2(\kappa,\tau)=\sum_{k=1}^{N/2}\left|\frac{\boldsymbol{P}(k)-\kappa\boldsymbol{S}(k)e^{j[\boldsymbol{\varphi}(k)-\boldsymbol{\theta}(k)+\boldsymbol{\mu}(k,\tau)]}}{\xi}\right|^2 \tag{10}$$

where ξ is the root mean square amplitude of the noise, and $E^2(\kappa,\tau)$ is the square accumulated error.

We simplify the above formula and replace the exponential expression with the trigonometric function expression. The simplified formula $E^2(\kappa,\tau)$ is given as follows:

$$E^2=\xi^{-2}\sum_{k=1}^{N/2}(\boldsymbol{P}_k^2+\kappa^2\boldsymbol{S}_k^2)+2\kappa\xi^{-2}\sum_{k=1}^{N/2}(\boldsymbol{P}_k\boldsymbol{S}_k\cos(\boldsymbol{\varphi}_k-\boldsymbol{\theta}_k+\boldsymbol{\mu}(k,\tau)) \tag{11}$$

where $E^2=E^2(\kappa,\tau)$, $\boldsymbol{P}_k=\boldsymbol{P}(k)$, $\boldsymbol{S}_k=\boldsymbol{S}(k)$, $\boldsymbol{\varphi}_k=\boldsymbol{\phi}(k)$, $\boldsymbol{\theta}_k=\boldsymbol{\theta}(k)$, $\boldsymbol{\mu}(k,\tau)$ is the phase difference. When E^2 reaches the minimum value, τ can be derived by calculating the partial derivative of (10). The partial derivative is shown as follows:

$$\frac{\partial E^2}{\partial\tau}=-\frac{2\kappa}{\xi^2}\sum_{k=1}^{N/2}\frac{\partial\boldsymbol{\mu}(k,\tau)}{\partial\tau}\boldsymbol{P}_k\boldsymbol{S}_k\sin(\boldsymbol{\varphi}_k-\boldsymbol{\theta}_k+\boldsymbol{\mu}(k,\tau)) \tag{12}$$

From (4) and (5), we know that $\mu(k,\tau)$ is non-linear

$$\boldsymbol{\theta}_k-\boldsymbol{\varphi}_k=\boldsymbol{\mu}(k,\tau)\neq-\frac{2\pi k\tau}{\ln\Lambda_b-\ln\Lambda_a} \tag{13}$$

As the velocimetry model with non-linear phase shift is difficult to establish, we need to build a phase dictionary of the non-periodic spectrum to eliminate the influence of nonlinear phase shift in Section 4.3.

B. LOW-FREQUENCY MEASUREMENT MATRIX WITH NDFT

A reasonably designed measurement matrix plays a significant role in the accurate reconstruction of the spectrum. A measurement matrix with good performance can reduce the running time of the algorithm while ensuring the accuracy of the reconstructed spectrum. The energy of the solar spectrum is generally concentrated in the low-frequency part of the Fourier matrix. In this section, L rows of the low-frequency part of NDFT is used as the measurement matrix. The low-frequency measurement matrix with NDFT, $\boldsymbol{\Phi}(L\times(N-2))$, is (14), as shown at the bottom of the page, where $\Delta\tau_n=\ln\lambda_{n+1}-\ln\lambda_{n-1}, n=1,2,3\ldots N-2$.

By using the measurement matrix $\boldsymbol{\Phi}$, the standard solar spectrum $\boldsymbol{s}$ and the measured spectrum $\boldsymbol{p}$, the zero-phase atom $\boldsymbol{\Theta}$ and the observation vector $\boldsymbol{\gamma}$ are

$$\boldsymbol{\Phi}=\frac{1}{2}\begin{bmatrix}\Delta\tau_1 & \Delta\tau_2 & \cdots & \Delta\tau_{N-2}\\ e^{-j\frac{2\pi\ln\lambda_1\bullet1}{\Lambda_b-\Lambda_a}}\Delta\tau_1 & e^{-j\frac{2\pi\ln\lambda_2\bullet1}{\Lambda_b-\Lambda_a}}\Delta\tau_2 & \cdots & e^{-j\frac{2\pi\ln\lambda_{N-2}\bullet1}{\Lambda_b-\Lambda_a}}\Delta\tau_{N-2}\\ e^{-j\frac{2\pi\ln\lambda_1\bullet2}{\Lambda_b-\Lambda_a}}\Delta\tau_1 & e^{-j\frac{2\pi\ln\lambda_2\bullet2}{\Lambda_b-\Lambda_a}}\Delta\tau_2 & \cdots & e^{-j\frac{2\pi\ln\lambda_{N-2}\bullet2}{\Lambda_b-\Lambda_a}}\Delta\tau_{N-2}\\ \vdots & \vdots & \ddots & \vdots\\ e^{-j\frac{2\pi\ln\lambda_1\bullet(L-1)}{\Lambda_b-\Lambda_a}}\Delta\tau_1 & e^{-j\frac{2\pi\ln\lambda_2\bullet(L-1)}{\Lambda_b-\Lambda_a}}\Delta\tau_2 & \cdots & e^{-j\frac{2\pi\ln\lambda_{N-2}\bullet(L-1)}{\Lambda_b-\Lambda_a}}\Delta\tau_{N-2}\end{bmatrix} \tag{14}$$

shown as follows:

$$\boldsymbol{\gamma} = \boldsymbol{\Phi} \bullet \boldsymbol{p} = \begin{bmatrix} \boldsymbol{P}(0)e^{j\boldsymbol{\theta}(0)} \\ \boldsymbol{P}(1)e^{j\boldsymbol{\theta}(1)} \\ \vdots \\ \boldsymbol{P}(L-1)e^{j\boldsymbol{\theta}(L-1)} \end{bmatrix} \tag{15}$$

$$\boldsymbol{\Theta} = \boldsymbol{\Phi} \bullet \boldsymbol{s} = \begin{bmatrix} \boldsymbol{S}(0)e^{j\varphi(\boldsymbol{\theta})} \\ \boldsymbol{S}(1)e^{j\boldsymbol{\varphi}\,(1)} \\ \vdots \\ \boldsymbol{S}(L-1)e^{j\boldsymbol{\varphi}(L-1)} \end{bmatrix} \tag{16}$$

The time complexity of the non-uniform discrete Fourier transform is $O(N^2)$. In practical applications (especially on the spacecraft), the non-uniform fast Fourier transform algorithm (nufft) can be used to do quick calculations [27], [28].

C. PHASE DICTIONARY OF NON-PERIODIC SPECTRUM

In order to construct a phase dictionary for a series of Doppler spectra, it is necessary to shift the standard spectrum at first. We save the results of the NDFT of the Doppler spectra.

1) DECOMPOSITION AND REPRESENTATION FOR CELESTIAL SPECTRUM

We need to generate a series of Doppler spectra based on the standard spectrum. For ensuring that the sampling point of the spectrum wavelength remains unchanged, the spectrum is divided into a series of cosine functions. $\boldsymbol{s}(\ln\lambda_n)$ is a one-dimensional discrete spectrum. The DCT of $\boldsymbol{s}(\ln\lambda_n)$ is shown as follows:

$$\boldsymbol{D}(0) = \frac{1}{\sqrt{N}} \sum_{\mathrm{n}=0}^{N-1} \boldsymbol{s}(\ln\lambda_n), \quad u = 0 \tag{17}$$

$$\boldsymbol{D}(u) = \sqrt{\frac{2}{N}} \sum_{n=0}^{N-1} \boldsymbol{s}(\ln\lambda_n) \cos[\frac{\pi}{2N}(2\frac{\lambda_n - \lambda_0}{R} + 1)u] \tag{18}$$

where $\boldsymbol{D}(u)$ is the u-th cosine transform coefficient, u is the generalized frequency variable, $u = 0, 1, 2, 3 \ldots N-1$.

The reconstructed spectrum using inverse cosine transform is shown as follows:

$$\boldsymbol{s}(\ln\lambda_n) = \frac{1}{\sqrt{N}}\boldsymbol{D}(0) + \sqrt{\frac{2}{N}} \sum_{u=1}^{N-1} \boldsymbol{D}(u) \cos[\frac{\pi}{2N}(2\frac{e^{\ln\lambda_n} - \lambda_0}{R} + 1)u] \tag{19}$$

2) CONSTRUCTION OF THE PHASE DICTIONARY

We suppose λ_0 is the initial wavelength of the spectrum, τ_i is the Doppler logarithmic factor, and R is the wavelength resolution. To generate the Doppler spectrum, all the cosine functions of the inverse cosine transform should be shifted:

$$\boldsymbol{s}^i(\ln\lambda_n) = \frac{1}{\sqrt{N}}\boldsymbol{D}(0) + \sqrt{\frac{2}{N}} \sum_{u=1}^{N-1} \boldsymbol{D}(u) \cos[\frac{\boldsymbol{\pi}}{2N}(2\frac{e^{\ln\lambda_n - \tau_i}}{R} - 2\frac{\lambda_0}{R} + 1)u] \tag{20}$$

where $\tau_i = \ln(1 + v_i/c)$. In order to generate a series of the Doppler spectrum, v_i is taken a series of specific values. Then we perform the non-uniform Fourier transform on this series of the spectrum, and save the transform results. We assume that $\boldsymbol{s}^i$ is the generated Doppler spectra, $\boldsymbol{S}^i$ and $\boldsymbol{\varphi}^i$ are the amplitude and phase of NDFT, respectively, $i = 1, 2, 3, \ldots, I$. The formed i-th atom, $\boldsymbol{\Theta}^i$, is expressed as follows:

$$\boldsymbol{\Theta}^i = \boldsymbol{\Phi} \bullet \boldsymbol{s}^i = \begin{bmatrix} \boldsymbol{S}^i(0)e^{j\boldsymbol{\varphi}^i(\theta)} \\ \boldsymbol{S}^i(1)e^{j\boldsymbol{\varphi}^i(1)} \\ \vdots \\ \boldsymbol{S}^i(L-1)e^{j\boldsymbol{\varphi}^i(L-1)} \end{bmatrix} \tag{21}$$

The formed dictionary is expressed as follows:

$$\boldsymbol{\Psi} = \begin{bmatrix} \boldsymbol{\Theta}^1 & \boldsymbol{\Theta}^2 & \cdots & \boldsymbol{\Theta}^i & \cdots & \boldsymbol{\Theta}^I \end{bmatrix} \tag{22}$$

D. NON-LINEAR AND SUPER-RESOLUTION MATCHING ALGORITHM

In (12), when $\boldsymbol{\phi}_k$ approaches $\boldsymbol{\theta}_k$, the value of $\frac{\partial \boldsymbol{\mu}(k,\tau)}{\partial \tau}$ can be approximately equal to $2\pi k/(\ln\Lambda_b - \ln\Lambda_a)$ as $\boldsymbol{\mu}(k,\tau)$ is nearly linear. The relationship between the phase of the i-th atom and the measured spectrum is shown as follows:

$$\boldsymbol{\varphi}_k^i + \boldsymbol{\mu}^i(k,\tau) = \boldsymbol{\theta}_k \tag{23}$$

where $\boldsymbol{\varphi}_k^i$ is the phase of the i-th atom, $\boldsymbol{\mu}^i(k,\tau)$ is the phase difference between the i-th atom and the measured spectrum. A matching formula based on dictionary atoms is shown as follows:

$$E_s^i = \sum_{k=0}^{L-1} k\boldsymbol{P}_k\boldsymbol{S}_k^i \sin(\boldsymbol{\varphi}_k^i - \boldsymbol{\theta}_k) \tag{24}$$

We match the NDFT result $\boldsymbol{\gamma}$ of the measured spectrum with the atoms, and calculate the similarity between $\boldsymbol{\gamma}$ and the atoms in the dictionary by (22). When the absolute value of E_s^i is the smallest, the corresponding atom is closest to $\boldsymbol{\gamma}$. The corresponding atomic number is shown as follows:

$$i = \arg\min_i \left| \sum_{k=0}^{L-1} k\boldsymbol{P}_k\boldsymbol{S}_k^i \sin(\boldsymbol{\varphi}_k^i - \boldsymbol{\theta}_k) \right| \tag{25}$$

And we can get more accurate velocity through the following relationship. The super-resolution algorithm for deriving the velocity is shown as follows:

$$\hat{\boldsymbol{\mu}}(k,\tau) = \begin{cases} \boldsymbol{\mu}^i(k,\tau) + (\boldsymbol{\varphi}_k^{i+1} - \boldsymbol{\varphi}_k^i)\dfrac{L_s^i}{L_s^{i+1} - L_s^i} & \text{if } L_s^i \cdot L_s^{i+1} < 0 \\ \boldsymbol{\mu}^i(k,\tau) + (\boldsymbol{\varphi}_k^i - \boldsymbol{\varphi}_k^{i-1})\dfrac{L_s^i}{L_s^i - L_s^{i-1}} & \text{if } L_s^i \cdot L_s^{i-1} < 0 \end{cases} \tag{26}$$

Finally, the RV can be derived according to the estimated value of phase shift.

In summary, the steps of the CSV-NFPS are shown as follows:

① The measurement matrix is designed, and the low-frequency part of the non-uniform Fourier transform is used as the measurement matrix.

② According to the measurement matrix, the vector matrix of the standard solar spectrum and the measured spectrum, the zero-phase atom and the observation vector are obtained.

③ The phase dictionary of the non-periodic spectrum is constructed. After a series of Doppler shifts of the standard solar spectrum, different atoms are obtained by using the NDFT, and then the dictionary is constructed.

④ The observation vector is matched with each atom in the dictionary, and the atom with the highest similarity is got. Finally, the velocity is derived by using the non-linear and super-resolution matching algorithm.

V. CRAMER-RAO LOWER BOUND OF THE CELESTIAL SPECTRUM VELOCITY

In signal estimation, the variance of unbiased estimation cannot be infinitely small. To evaluate the accuracy of the proposed method, the CRLB for velocity estimation is given. We assume that $\boldsymbol{s}(\ln\lambda_n)$ is the original spectrum, and $\boldsymbol{s}(\ln\lambda_n - \tau)$ is the Doppler spectrum with an unknown parameter τ, and $\boldsymbol{\omega}(n)$ is the Gaussian white noise with a standard deviation of σ. The relation between them is shown as follows:

$$\boldsymbol{p}(ln\lambda_n) = \boldsymbol{s}(ln\lambda_n - \tau) + \boldsymbol{\omega}(n) \quad n = 0, 1, 2, \ldots, N-1 \tag{27}$$

Its probability likelihood function is given as follows:

$$L(p;\tau) = \frac{1}{(2\pi\sigma^2)^{\frac{N}{2}}} \exp \times \left\{ -\frac{1}{2\sigma^2} \sum_{n=0}^{N-1} [\boldsymbol{p}(ln\lambda_n) - \boldsymbol{s}(ln\lambda_n - \tau)]^2 \right\} \tag{28}$$

The first partial derivative of τ is given as follows:

$$\frac{\partial \ln L(p;\tau)}{\partial \tau} = \frac{1}{\sigma^2} \times \sum_{n=0}^{N-1} [\boldsymbol{p}(ln\lambda_n) - \boldsymbol{s}(ln\lambda_n - \tau)] \frac{\partial \boldsymbol{s}(ln\lambda_n - \tau)}{\partial \tau} \tag{29}$$

The second partial derivative of τ is given as follows:

$$\frac{\partial^2 \ln L(p;\tau)}{\partial \tau^2} = \frac{1}{\sigma^2} \sum_{n=0}^{N-1} [\boldsymbol{p}(ln\lambda_n) - \boldsymbol{s}(ln\lambda_n - \tau)] \frac{\partial^2 \boldsymbol{s}(ln\lambda_n - \tau)}{\partial \tau^2} - \frac{1}{\sigma^2} \left[\frac{\partial \boldsymbol{s}(ln\lambda_n - \tau)}{\partial \tau} \right]^2 \tag{30}$$

The mathematical expectation of $\boldsymbol{s}(\ln\lambda_n)$ is shown as follows:

$$E\left[\frac{\partial^2 \ln L(p;\tau)}{\partial \tau^2} \right] = -\frac{1}{\sigma^2} \sum_{n=0}^{N-1} \left[\frac{\partial \boldsymbol{s}(ln\lambda_n - \tau)}{\partial \tau} \right]^2 \tag{31}$$

From (20), the specific form of $\frac{\partial \boldsymbol{s}(ln\lambda_n - \tau)}{\partial \tau}$ is given as follows:

$$\frac{\partial \boldsymbol{s}(ln\lambda_n - \tau)}{\partial \tau} = \sqrt{\frac{2}{N}} \sum_{u=0}^{N-1} e^{\ln\lambda_n - \tau} u \frac{\pi}{RN} \boldsymbol{D}(u) \sin \times \left[\frac{\pi}{2N} (2\frac{e^{\ln\lambda_n - \tau} - \lambda_0}{R} + 1)u \right] \tag{32}$$

where $\boldsymbol{D}(u)$ is the discrete cosine transform of $\boldsymbol{s}(\ln\lambda_n)$.

The CRLB of the estimate of τ is shown as follows:

$$var(\hat{\tau}) \geq \frac{\sigma^2}{\sum_{n=0}^{N-1} \left[\frac{\partial \boldsymbol{s}(ln\lambda_n - \tau)}{\partial \tau} \right]^2} = \frac{\sigma^2}{\frac{2\pi^2}{N^3} \sum_{n=0}^{N-1} \left\{ \sum_{u=0}^{N-1} e^{\ln\lambda_n - \tau} \frac{u}{R} \boldsymbol{D}(u) \sin \left[\frac{\pi}{2N} (2\frac{e^{\ln\lambda_n - \tau} - \lambda_0}{R} + 1)u \right] \right\}^2} \tag{33}$$

where $\tau = \ln(1 + v/c)$.

The CRLB of the estimate of v is shown as follows:

$$var(\hat{v}) \geq \frac{\sigma^2 \left(\frac{dv}{d\tau}\right)^2}{\sum_{n=0}^{N-1} \left[\frac{\partial \boldsymbol{s}(ln\lambda_n - \tau)}{\partial \tau} \right]^2} = \frac{\sigma^2 c^2 \left(1 + \frac{v}{c}\right)^4}{\frac{2\pi^2}{N^3} \sum_{n=0}^{N-1} \left\{ \left\{ \sum_{u=0}^{N-1} \lambda_n \frac{u}{R} \boldsymbol{D}(u) \sin \left[\frac{\pi}{2N} (2\frac{\frac{c\lambda_n}{c+v} - \lambda_0}{R} + 1)u \right] \right\} \right\}^2} \tag{34}$$

From (34), we find some properties as follows:

① The CRLB is proportional to the variance of the noise, σ^2.

② The CRLB decreases with the $\boldsymbol{D}(u)$. The $\boldsymbol{D}(u)$ of reflected light from different planets are different, and the corresponding CRLB is also different.

③ With the increase of the RV, the CRLB increases slightly. The reason is that v is much smaller than the speed of light.

VI. EXPERIMENTAL RESULTS

In this section, we compare the NDFT Taylor method with the CSV-NFPS. The effects of noise level, the atomic interval, the number of spectral lines, the degree of spectral aberrance, the wavelength range and the reflectivity on the CSV-NFPS are also analyzed.

A. SIMULATION CONDITIONS

In the selection of the standard spectrum, it is necessary to select the spectrum during the tranquil stages of solar activity. The number of solar photons in the sun in 2018 is small, so the spectrum in 2018 is selected as the standard spectrum. The solar spectrum data can be obtained from the astronomy

website of Chile [29]. The parameters of the solar spectrum used in this experiment are shown in Table 1.

TABLE 1. Parameters of the solar spectrum data.

Name	Parameter
Wavelength range	[gte:378.193nm, lte:691.301nm]
Observatory	La Silla Paranal APEX
Data collection	ESO, PHASE3
Observation date	2018-04-08 21:07:12

The range of the second half of the spectrum is from 538.192nm to 691.192nm. We set the theoretical velocity of the spacecraft to 9750m/s, and generate the corresponding Doppler spectrum. If not stated, the flux noise is the Gaussian white noise with standard deviation $\boldsymbol{\sigma} = 1000\text{erg/s/cm}^2\text{/angstrom}$. The unit of the noise amplitude is the same as the spectral flux, namely erg/s/cm^2/angstrom. The experiments were carried out on a Hasee notebook with an Intel Core i7-10750H CPU @ 2.60 GHz and 8 GB RAM.

B. CRAMER-RAW LOWER BOUND (CRLB)

In order to reflect the superiority of the CSV-NFPS, we compared its accuracy with CRLB. Table 2 shows the accuracy of the CSV-NFPS and its CRLB with different noises. The value of CRLB increases with the noise level. And the two of them are of proportional relation. As can be seen from Table 2, there is a small room for improvement of accuracy. It shows that our velocimetry accuracy is very close to the CRLB values with different noise levels.

Table 3 shows the effect of the spacecraft velocity on CRLB. With the same noise level, CRLB slightly increases with the velocity. As the spacecraft velocity is much smaller than the velocity of light, the variation of the spacecraft velocity has little effect on CRLB.

The spectrum used for navigation can also come from other planets or asteroids (reflected light from the sun) [30]. We select the spectrum of reflected light of celestial bodies, whose parameters are the same as Table 1 except for the observation time. These reflection spectrum data can be obtained on the Astronomy website of Chile [29]. These reflection spectra are used to investigate the effect of $\boldsymbol{D}(u)$ on CRLB. Table 4 shows the velocity estimated errors using spectra of the reflected light. It can be seen that the velocimetry accuracy is close to CRLB.

Figure 2 shows the amplitude-frequency of different reflection spectra from the output of DCT. We can see that the four groups of reflection spectra are similar in frequency components, and the difference is in the size of frequency amplitude. The frequency amplitude of spectra of Io and Moon is larger than the other two groups, so their CRLB is smaller. The reason is that the CRLB increases with the $\boldsymbol{D}(u)$, which is consistent with (34). In addition to direct sunlight, we can select a spectrum of strong reflected light for navigation.

C. THE NUMBER OF NDFT SPECTRAL LINES

The celestial velocimetry method on spacecraft has high requirements for timeliness. On the one hand, in the CSV-NFPS, the number of NDFT spectral lines is in proportion to the computational load. On the other hand, the number of NDFT spectral lines is related to velocimetry accuracy. Therefore, the number of Fourier spectral lines makes a good compromise between velocimetry accuracy and computational load.

Figure 3 shows the velocimetry error vs. the number of spectral lines. It can be seen from Figure 3 that when the number of the NDFT spectral lines changes from 1000 to 16000, the error decreases rapidly; when the number of frequency spectrum lines varies from 16000 to 20000, the error decreases slowly and reaches the lowest value at 20000. When the number of NDFT spectral lines is larger than 20000, the velocimetry error tends to be stable. The square root of CRLB is 0.966m/s. When the number of NDFT spectral lines is 20000, the velocimetry error is 0.987m/s, which is close to the square root of CRLB. Therefore, we select 20000 spectral lines.

D. ATOMIC INTERVAL

The atomic interval affects the velocimetry accuracy, computational load and storage space. In this section, we investigate the effect of atomic interval on velocimetry. The NDFT result files based on the original frequency spectrum shifted from 8800m/s to 10400m/s are generated.

The velocimetry error, running time and dictionary size are shown in Table 5. It can be seen that during the atomic interval change from 50m/s to 100m/s, the velocimetry error does not change significantly. When the atomic interval exceeds 100m/s, the velocimetry error increases with the atomic interval. As the atomic interval increasing, the running time becomes shorter, and the dictionary size gradually decreases. Therefore, we choose 100m/s as the experimental atomic interval, which reduces the amount of calculation and the requirement of storage space while ensuring accuracy.

E. THE NDFT TAYLOR METHOD

We compare the CSV-NFPS with the NDFT Taylor method that is a classical velocimetry algorithm. As the velocimetry accuracy is related to the velocity, we set different preset velocities, v_p. The velocity search range of the two methods is from $v_p - 100$(m/s) to $v_p + 100$(m/s). The running time here is the time operating on the spacecraft. The searching step of the NDFT Taylor method is 0.03m/s.

It can be seen from Table 6 that when the RV is smaller than 1km/s, the non-linear bias of the NDFT Taylor method is approximately 0.01m/s; when the RV reaches 10km/s, the non-linear bias of the NDFT Taylor method is on the order of 0.1m/s, which affects the performance of the velocimetry navigation. The CSV-NFPS almost eliminates the non-linear

TABLE 2. The CRLB and the estimation errors with different noise levels.

Noise level (erg/s/cm^2/angstrom)	100	1000	3000	5000	10000
√CRLB (m/s)	0.0966	0.966	2.898	4.830	9.660
Estimation error(m/s)	0.0986	0.987	3.067	5.080	10.070
Improvement	2.07%	2.07%	5.83%	5.18%	4.24%

TABLE 3. The CRLB with different v and different noise levels.

Noise level (erg/s/cm^2/angstrom) \ v(m/s)	1	10	100	1000	10000
100	0.00933	0.00933	0.00933	0.00933	0.00933
1000	0.93302	0.93302	0.93302	0.93303	0.93306
10000	93.30211	93.30212	93.30221	93.30294	93.30574

TABLE 4. Velocity estimation error using planetary spectrum and their CRLB.

Name	Velocimetry error(m/s)	√CRLB	Observation time
Europa	8.1668	6.4930	2014-01-07 03.00.31
Ganymede	7.1148	5.8596	2007-04-13 09.31.44
Io	1.4947	1.4110	2007-09-30 00.51.29
Moon	2.3281	2.1841	2016-04-01 08:20:10

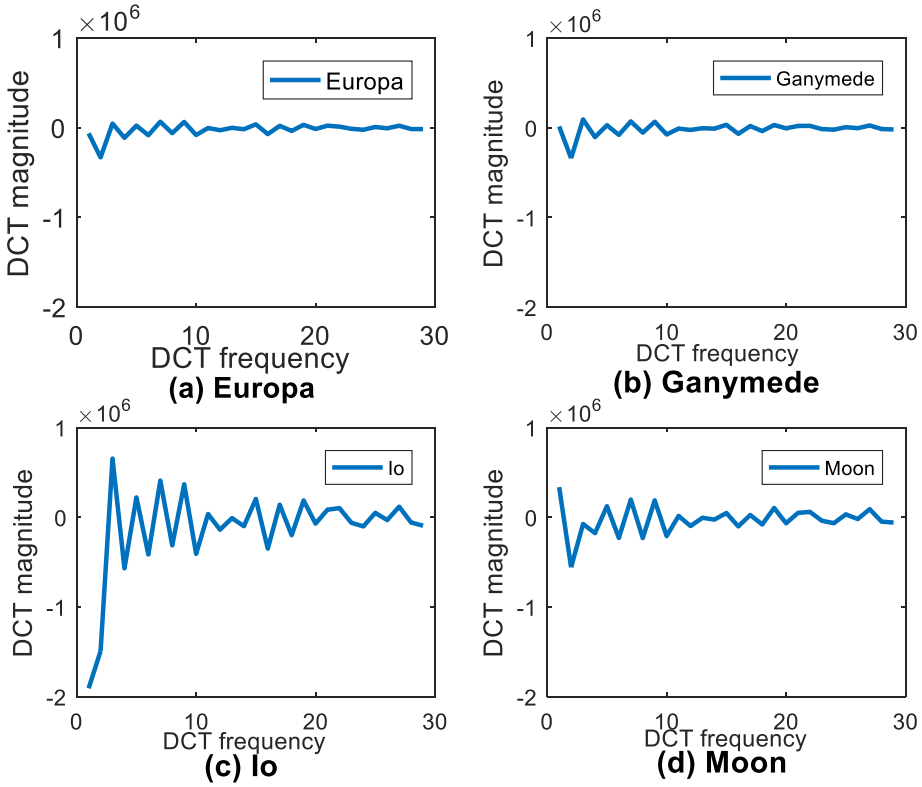

FIGURE 2. DCT of four groups of spectra.

bias. The residual is on the order of 10^{-5}m/s, which has no effect on the performance of the velocimetry navigation. The reason is that the non-linear phase shift is approximated by the phase dictionary of the non-periodic spectrum. Besides, the running time of the CSV-NFPS with non-linear Fourier phase shift is less than that of the NDFT Taylor method.

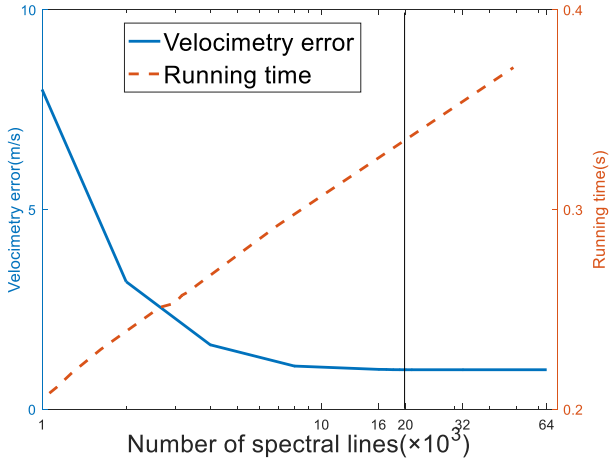

FIGURE 3. Velocimetry error and running time with different numbers of spectral lines.

TABLE 5. Velocity estimation performance with different atomic intervals.

Atomic interval (m/s)	Velocimetry error (m/s)	Running time (s)	Dictionary size (kb)
50	0.987	6.571	15675
100	0.987	3.596	8075
200	0.988	1.984	4275
400	0.997	1.183	2375
800	1.181	0.798	1425
1600	2.8192	0.595	950

TABLE 6. NDFT Taylor method vs. CSV-NFPS (without noise).

Preset velocity v_p(m/s)	NDFT Taylor Method		CSV-NFPS	
	bias (m/s)	Running time (s)	bias (m/s)	Running time (s)
1	0.01		0.000001	
10	0.01		0.000001	
100	0.01	1.145	0.000008	0.858
1000	0.009		0.000003	
10000	0.143		0.000033	

The reason is that the large atomic interval and super-resolution matching algorithm reduces the number of searches greatly, while in the NDFT Taylor method, the searching step is short, and the number of searches is large.

Table 7 shows the comparison between the NDFT Taylor method and the CSV-NFPS with different noise levels. The search interval of both methods is from 9650m/s to 9850m/s.

It can be seen from Table 7 that with the different noise levels, the CSV-NFPS is better than the NDFT Taylor method

TABLE 7. NDFT Taylor method vs. CSV-NFPS (with noise).

Noise level (erg/s/cm^2/angstro-m)	NDFT Taylor method		CSV-NFPS	
	Velocimetr y error (m/s)	Runnin g time (s)	Velocimetr y error (m/s)	Runnin g time (s)
1000	1.039		0.987	
3000	3.184	1.142	3.067	0.856
5000	5.238		5.078	

in terms of velocimetry accuracy and running time. The above simulation results confirm the superiority of the CSV-NFPS.

F. WAVELENGTH RESOLUTION OF THE CELESTIAL SPECTRUM

The wavelength resolution is also an essential factor in velocimetry navigation. High resolution is conducive to improving the velocimetry accuracy, while a low resolution is conducive to reducing the requirements for the spectrometer. In this section, we investigate the effect of spectral resolution on velocimetry.

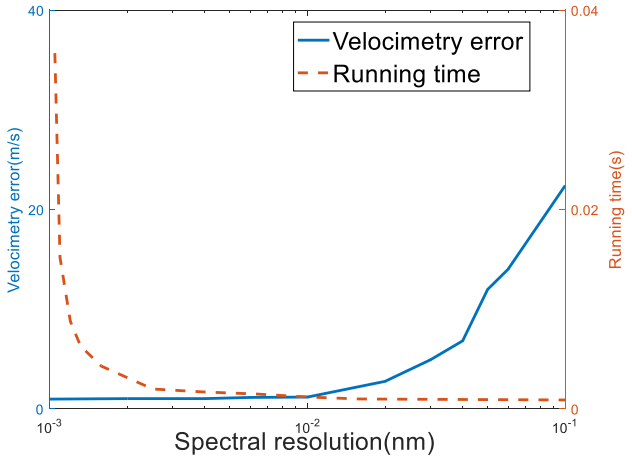

FIGURE 4. Velocimetry error and running time with different resolutions.

Figure 4 shows the relationship among the wavelength resolution, velocimetry error and running time. In the process of reducing the resolution from 0.001nm to 0.01nm, the velocimetry error of the CSV-NFPS does not change significantly, and the running time is largely reduced. In the process of reducing the resolution from 0.01nm to 0.1nm, the velocimetry error of the CSV-NFPS increases significantly, and the running time remained almost unchanged. The reason is that the transform domain method is little affected by the time resolution. In practical application, the 0.01nm spectral resolution makes a good compromise between velocimetry accuracy and requirements for the spectrometer, which can reduce the resolution of the spectrometer.

G. FREQUENCY ABERRANCE

Solar activities, such as flares and prominences can distort the spectral frequency, seriously affect the velocimetry accuracy. The frequency fluctuation of the spectrum is also an important part that affects the performance of velocimetry. In this section, we investigate the influence of spectral frequency aberrance on velocimetry accuracy.

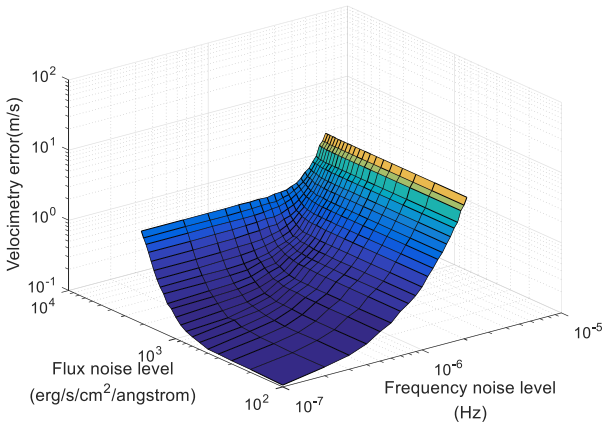

FIGURE 5. The relationship among the velocimetry error, the flux noise level, and the frequency noise level.

Figure 5 shows the effect of the flux noise level and the frequency aberrance on the velocimetry accuracy. It can be seen from Figure 5 that the shape of velocimetry error is a curved quadrilateral. The velocimetry error increases with both the flux noise level and the frequency aberrance. Moreover, the influence of the frequency aberrance on the velocimetry accuracy is more obvious than the flux noise. Therefore, in practical application, we select celestial spectrum with a more stable frequency for navigation.

H. REFLECTIVITY

When the celestial spectrum used for navigation comes from the reflected light of other planets or asteroids, the surface reflectivity of the planet or asteroid to sunlight also affect the performance of velocimetry. In this section, considering this factor, we analyze the influence of reflectivity on velocimetry accuracy. We assume that planets or asteroids have the same reflectivity for all wavelengths of sunlight.

As can be seen from Figure 6, with the same noise level, the velocimetry error gradually decreases with the increase of reflectivity. The reason is that the signal-to-noise ratio increases with reflectivity, and the velocimetry accuracy increases with the signal-to-noise ratio. Therefore, it is appropriate to select the spectrum of a planet or asteroid with high reflectivity as the celestial optical information for navigation.

I. WAVELENGTH RANGE

In this section, we investigate the effects of wavelength ranges on velocimetry. The short wavelength range of the spectrometer is benefit to reduce the load of the spectrometer.

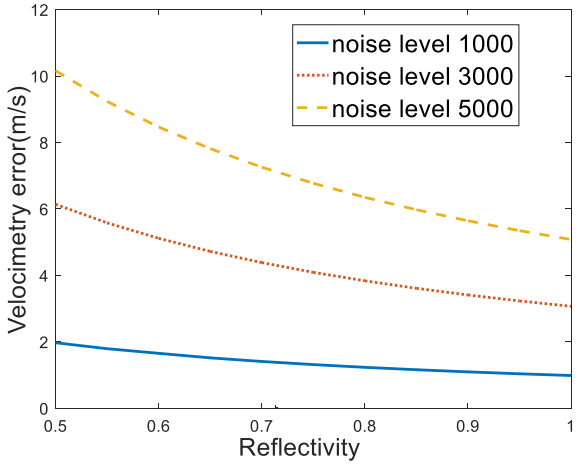

FIGURE 6. The relationship among velocimetry error, flux noise level and reflectivity.

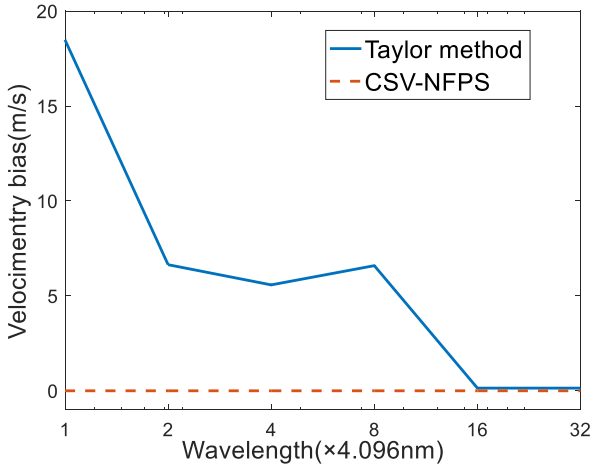

FIGURE 7. NDFT Taylor method vs. CSV-NFPS with different wavelength ranges.

In Figure 7, it can be seen that with different wavelength ranges, the CSV-NFPS has further smaller biases than the NDFT Taylor method. The velocimetry bias of the NDFT Taylor method decreases with the wavelength range, while the CSV-NFPS ensures very small biases with different wavelength ranges. This demonstrates that the CSV-NFPS eliminates the non-linear biases. The reason is that the non-linear phase shift is approximated by the phase dictionary of the non-periodic spectrum. The short wavelength range declines our requirements for spectrometers.

We use the measured Ceres spectra to verify the effectiveness of the CSV-NFPS. Due to the lack of the real RV value, we can only take a different approach to evaluate the velocimetry accuracy of the measured spectra. Theoretically, the mean RV of all pieces, RV_m, and the RV derived by computing the whole spectrum, RV_h, is equal. The difference between the RV_m and the RV_h reflect the non-linear bias. And the standard deviation of the RV of all pieces, σ_{RV} also reflect the velocimetry accuracy. The Ceres spectrum, whose observation time is 2015-08-28 6.03.37, is adopted as the

TABLE 8. RV measurements obtained with ceres.

Observation Time	2015-07-31 00.32.07		2015-07-31 02.22.42		2015-07-31 03.05.05		2015-07-31 03.18.36	
Method	Taylor	CSV-NFPS	Taylor	CSV-NFPS	Taylor	CSV-NFPS	Taylor	CSV-NFPS
RV_h(m/s)	-3091.18	-3103.96	-3078.58	-3090.42	-3080.98	-3092.24	-3078.58	-3088.23
RV_m(m/s)	-3099.67	-3103.04	-3082.90	-3089.92	-3088.60	-3090.47	-3084.37	-3086.89
Difference(m/s)	8.49	-0.92	4.32	-0.5	7.62	-1.77	5.79	-1.34
σ_{RV}(m/s)	27.39	24.25	25.41	16.35	14.29	13.48	20.12	17.71

template spectrum. The wavelength range of each piece is 4.096nm.

In Table 8, we list the observation time of the object spectrum, RV of the whole spectrum, the mean RV of all pieces, the standard deviation, and the Observation date. In the four experiments, RV_h and RV_m derived by the CSV-NFPS are approximately equal, while the difference between RV_h and RV_m derived by the NDFT Taylor method is large. In addition, for different spectra, the CSV-NFPS has a smaller standard deviation than the NDFT Taylor method. The above experiment results confirm that the CSV-NFPS eliminates the non-linear bias in a short wavelength range. A short-wavelength range means a small spectrometer load.

VII. CONCLUSION

A novel celestial spectrum velocimetry method with non-linear Fourier phase shift is proposed in this paper. In this method, we use the low-frequency Fourier measurement matrix, the phase dictionary of the non-periodic spectrum, and the non-linear and super-resolution matching algorithm to construct the CS with non-linear Fourier phase shift. And we estimate the Fourier phase shift between the spacecraft and the navigation star through the CS with non-linear phase shift. According to the simulation results, conclusions can be drawn as follows:

① High accuracy and real-time. As the effect of a wavelength shift on a spectrum is to introduce its transform a non-linear Fourier phase shift, the CSV-NFPS use the phase dictionary of the non-periodic spectrum to approach the non-linear Fourier phase shift. Long atomic interval (100m/s) and the super-resolution matching algorithm decrease the number of searches greatly, and improve real-time performance. The CSV-NFPS proposed in this paper is superior to the NDFT Taylor method in terms of accuracy and computational complexity. Besides, the number of Fourier spectral lines makes a good compromise between velocimetry accuracy and running time.

② Low requirements for the spectrometer. On the one hand, to reach 1m/s velocimetry accuracy, the wavelength resolution of the spectrometer only requires 0.01nm. The wavelength resolution of the HARPS in Chile is 0.001nm. Thus, our requirements for the wavelength resolution of the spectrometer is low. On the other hand, the short wavelength range leads to a large non-linear velocimetry bias in the NDFT Taylor method. However, the CSV-NFPS is robust to this non-linear velocimetry bias, and ensures a high accuracy with a short wavelength range. Thus, the CSV-NFPS has low requirements for the wavelength resolution of the spectrometer.

To sum up, the CSV-NFPS has high accuracy, real-time, and low requirements for the spectrometer. The CSV-NFPS is suitable for the celestial velocimetry navigation.

In the future work, we will consider the effects of planetary surface reflectivity and atmospheric absorptivity on Doppler velocimetry in detail. At the same time, we will strive to improve the velocimetry performance of our method under low signal-to-noise. Our algorithm will be further improved in a large number of measured spectra.

REFERENCES

[1] L. Gerdes, M. Azkarate, J. R. Sánchez-Ibáñez, L. Joudrier, and C. J. Perez-del-Pulgar, "Efficient autonomous navigation for planetary rovers with limited resources," *J. Field Robot.*, vol. 37, no. 7, pp. 1153–1170, Aug. 2020.

[2] N. Hacene and B. Mendil, "Behavior-based autonomous navigation and formation control of mobile robots in unknown cluttered dynamic environments with dynamic target tracking," *Int. J. Autom. Comput.*, vol. 18, no. 5, pp. 766–768, Mar. 2021.

[3] X. Chen, Z. Sun, W. Zhang, and J. Xu, "A novel autonomous celestial integrated navigation for deep space exploration based on angle and stellar spectra shift velocity measurement," *Sensors*, vol. 19, no. 11, p. 2555, Jun. 2019.

[4] G. Ma and W. You, "A Hardware-in-the-loop simulation system of deep space autonomous navigation based on angle and velocity measurement," in *Proc. Chin. Control Decis. Conf. (CCDC)*, Aug. 2020, pp. 3779–3783.

[5] L. Huang, P. Shuai, X. Zhang, and S. Chen, "A new explorer mission for soft X-ray timing–observation of the crab pulsar," *Acta Astronautica*, vol. 151, pp. 63–67, Oct. 2018.

[6] Y. Wang, W. Zheng, and D. Zhang, "X-ray pulsar/starlight Doppler deeply-integrated navigation method," *J. Navigat.*, vol. 70, no. 4, pp. 829–846, Mar. 2017.

[7] J. Liu, Y. Li, X. Ning, X. Chen, and Z. Kang, "Modeling and analysis of solar Doppler difference bias with arbitrary rotation axis," *Chin. J. Aeronaut.*, vol. 33, no. 12, pp. 3331–3343, Dec. 2020.

[8] E. G. Lightsey, A. E. Mogensen, P. D. Burkhart, T. A. Ely, and C. Duncan, "Real-time navigation for Mars missions using the Mars network," *J. Spacecraft Rockets*, vol. 45, no. 3, pp. 519–533, May 2008.

[9] J.-H. Hong, W. Park, and C.-K. Ryoo, "An autonomous space navigation system using image sensors," *Int. J. Control, Autom. Syst.*, vol. 19, no. 6, pp. 2122–2133, Mar. 2021.

[10] X. Ning, M. Gui, J. Fang, G. Liu, and W. Wu, "A novel autonomous celestial navigation method using solar oscillation time delay measurement," *IEEE Trans. Aerosp. Electron. Syst.*, vol. 54, no. 3, pp. 1392–1403, Jun. 2018.

[11] J. Liu, X.-L. Ning, X. Ma, and J.-C. Fang, "Geometry error analysis in solar Doppler difference navigation for the capture phase," *IEEE Trans. Aerosp. Electron. Syst.*, vol. 55, no. 5, pp. 2556–2567, Oct. 2019.
[12] Y. Li and A. Zhang, "Observability analysis and autonomous navigation for two satellites with relative position measurements," *Acta Astronautica*, vol. 163, pp. 77–86, Oct. 2019.
[13] M. Zhang, K. Li, B. Hu, and C. Meng, "Comparison of Kalman filters for inertial integrated navigation," *Sensors*, vol. 19, no. 6, p. 1426, 2019.
[14] J. Liu, X.-L. Ning, X. Ma, J.-C. Fang, and G. Liu, "Direction/distance/velocity measurements deeply integrated navigation for Venus capture period," *J. Navigat.*, vol. 71, no. 4, pp. 861–877, Feb. 2018.
[15] J. Liu, J.-C. Fang, Z.-H. Yang, Z.-W. Kang, and J. Wu, "X-ray pulsar/Doppler difference integrated navigation for deep space exploration with unstable solar spectrum," *Aerosp. Sci. Technol.*, vol. 41, pp. 144–150, Feb. 2015.
[16] W. Zhang, Q. Huang, and X. Chen, "Autonomous celestial navigation method of asteroid probe based on angle measurement and velocity measurement," *SCIENTIA SINICA Phys., Mech. Astronomica*, vol. 49, no. 8, Aug. 2019, Art. no. 084510.
[17] R. G. Franklin and D. L. Birx, "A study of natural electromagnetic phenomena for space navigation," *Proc. IRE*, vol. 48, no. 4, pp. 532–541, Apr. 1960.
[18] A. C. Cameron, A. Mortier, D. Phillips, X. Dumusque, R. D. Haywood, N. Langellier, and C. A. Watson, "Three years of Sun-as-a-star radial-velocity observations on the approach to solar minimum," *Monthly Notices Roy. Astron. Soc.*, vol. 487, no. 1, pp. 1082–1100, Jul. 2019.
[19] G. Anglada-Escudé and R. P. Butler, "The HARPS-TERRA project. I. Description of the algorithms, performance, and new measurements on a few remarkable stars observed by HARPS," *Astrophys. J. Suppl. Ser.*, vol. 200, no. 2, p. 15, May 2012.
[20] M. Zechmeister, A. Reiners, P. J. Amado, M. Azzaro, F. F. Bauer, V. J. S. Béjar, and J. A. Caballero, "Spectrum radial velocity analyser (SERVAL): High-precision radial velocities and two alternative spectral indicators," *Astron. Astrophys.*, vol. 609, p. A12, Jan. 2018.
[21] D. R. Wilkins, "Low-frequency X-ray timing with Gaussian processes and reverberation in the radio-loud AGN 3C 120," *Monthly Notices Roy. Astron. Soc.*, vol. 489, no. 2, pp. 1957–1972, Oct. 2019.
[22] Z. Wang, X. Huang, J. Liu, X. Ma, and X. Chen, "Stellar spectrum-based relative velocimetry with spectrometer and its integrated navigation," *Optik*, vol. 207, Apr. 2020, Art. no. 163805.
[23] J. Zhang, J. Liu, X. Ma, Z.-W. Kang, and Z.-N. Wang, "Real-time and highly accurate solar spectrum velocimetry using the mirror NDFT-CS for Doppler navigation," *J. Aerosp. Eng.*, vol. 34, no. 6, Nov. 2021, Art. no. 04021091.
[24] J. H. Taylor, "Pulsar timing and relativistic gravity," *Philos. Trans. Roy. Soc. London, Ser. A, Phys. Eng. Sci.*, vol. 341, no. 1660, pp. 117–134, 1992.
[25] M. Lotfi and M. Vidyasagar, "A fast noniterative algorithm for compressive sensing using binary measurement matrices," *IEEE Trans. Signal Process.*, vol. 66, no. 15, pp. 4079–4089, Aug. 2018.
[26] P. Bao, H. Sun, Z. Wang, Y. Zhang, W. Xia, K. Yang, W. Chen, M. Chen, Y. Xi, S. Niu, J. Zhou, and H. Zhang, "Convolutional sparse coding for compressed sensing CT reconstruction," *IEEE Trans. Med. Imag.*, vol. 38, no. 11, pp. 2607–2619, Nov. 2019.
[27] A. Dutt and V. Rokhlin, "Fast Fourier transforms for nonequispaced data," *SIAM J. Sci. Comput.*, vol. 14, no. 6, pp. 1368–1393, 1993.
[28] S. F. Potter, N. A. Gumerov, and R. Duraiswami, "Fast interpolation of bandlimited functions," in *Proc. IEEE Int. Conf. Acoust., Speech Signal Process. (ICASSP)*, New Orleans, LA, USA, Mar. 2017, pp. 4516–4520.
[29] *ESO HARPS Archive*. Accessed: May 2021. [Online]. Available: http://archive.eso.org/scienceportal/home
[30] A. F. Lanza, P. Molaro, L. Monaco, and R. D. Haywood, "Long-term radial-velocity variations of the Sun as a star: The HARPS view," *Astron. Astrophys.*, vol. 587, p. A103, Mar. 2016.

ZIJUN ZHANG was born in Jingzhou, China, in October 1999. He is currently pursuing the Ph.D. degree with the Wuhan University of Science and Technology. His research interest includes autonomous celestial navigation.

JIN LIU was born in Lengshuijiang, China, in October 1981. He received the Ph.D. degree in pattern recognition and intelligent system from the Huazhong University of Science and Technology, in 2011.

He has completed his postdoctoral experience from Beihang University, in 2015. Currently, he is a Professor with the Wuhan University of Science and Technology. His research interest includes autonomous celestial navigation.

XIAOLIN NING was born in Jinan, China, in January 1979. She received the B.E. degree in computer science from Shandong Teachers University, Shandong, China, in 2001, and the Ph.D. degree in mechanical engineering from the Beijing University of Aeronautics and Astronautics (now Beihang University), Beijing, China, in 2008.

She has been a Professor with the School of Instrumentation and Optoelectronic Engineering, Beihang University, since 2018. Her research interests include guidance, navigation, and control system of spacecraft and autonomous navigation of deep-space explorers.